

Rationally Reconstructed Metal-organic Frameworks as Robust Oxygen Evolution Electrocatalysts

Chengxu Zhang

Kunming University of Science and Technology

Qianglong Qi

Kunming University of Science and Technology

Yunjie Mei

Kunming University of Science and Technology

Jue Hu

Kunming University of Science and Technology <https://orcid.org/0000-0002-0821-3874>

Mingzi Sun

Hong Kong Polytechnic University <https://orcid.org/0000-0001-5136-7265>

Yingjie Zhang

Kunming University of Science and Technology

Bolong Huang

Hong Kong Polytechnic University <https://orcid.org/0000-0002-2526-2002>

Libo Zhang

Kunming University of Science and Technology

Shihe Yang (✉ chsyang@pku.edu.cn)

Peking University Shenzhen

Article

Keywords: Metal-organic frameworks, Reconstruction, Electrocatalysis, Oxygen evolution reaction, Real-time kinetic simulation

Posted Date: August 11th, 2022

DOI: <https://doi.org/10.21203/rs.3.rs-1953017/v1>

License:   This work is licensed under a Creative Commons Attribution 4.0 International License.

[Read Full License](#)

Abstract

Although the metal-organic framework (MOF) based materials have become one of the most important types of electrocatalysts for the sluggish oxygen evolution reaction (OER), a novel design strategy for the MOF structure is highly needed to overcome the current development bottleneck of the electrochemical performance. Reconstructing MOFs towards a designed framework structure provides breakthrough opportunities to achieve unprecedented OER electrocatalytic performance, but has rarely, if ever, been proposed and investigated yet due to the significant challenges during the synthesis. Here, we report the first successful fabrication of a robust OER electrocatalyst by precision reconstruction of an MOF structure from MOF-74-Fe to MIL-53(Fe)-2OH with different coordination environments at the active sites. Theoretical calculations have revealed that the Fe sites in MIL-53(Fe)-2OH with uncoordinated phenolic hydroxyls are more electroactive than that in MOF-74-Fe. Benefiting from this desired electronic structure, the designed MIL-53(Fe)-2OH catalyst exhibits unprecedentedly high intrinsic OER activity, including a low overpotential of 215 mV at 10 mA cm⁻², low Tafel slope of 45.4 mV dec⁻¹ and high turnover frequency (TOF) of 1.44 s⁻¹ at the overpotential of 300 mV, which is 81 times higher than the TOF of the commercial IrO₂ catalyst (0.0177 s⁻¹). The radically reduced eg-t_{2g} crystal field splitting in Fe-3d and thus the much suppressed electron hopping barriers through the synergistic effects of the O species from the coordinated carboxyl groups and the uncoordinated phenolic groups guarantee the efficient OER in MIL-53(Fe)-2OH. Consistent with the DFT calculations, the real-time kinetic simulation reveals that the conversion from O* to OOH* is the rate-determining step on the active sites of MIL-53(Fe)-2OH. This work establishes a MOF platform to systematically investigate the structure-property relationship for rationally designing and fabricating robust OER electrocatalysts in the future.

Introduction

Metal-organic frameworks (MOFs) are a type of crystalline porous materials, which have become competitive oxygen evolution reaction (OER) catalysts largely due to their inherent high porosity and surface area as well as their designability.^{1,2} Understanding the structure-property relationship is crucial for enhancing the activity and durability of the catalysts for different electrochemical reactions in different environments.^{3,4} Although the significance of the electrocatalytic structure-property dependency has been well established for the pyrolyzed MOF materials, such dependency for the MOFs in their pristine or near pristine forms is still unclear, which entails an even more vast exploration space for modulating the structure and catalytic performance of these inherently porous and molecularly ordered materials. Two main strategies have been taken to accelerate the sluggish four-electron OER process on MOF catalysts. One is to fabricate nanostructured MOFs with coordinatively unsaturated metal sites, such as ultrathin MOF nanosheets,⁵ nanotubular arrays,⁶ or defect-rich MOFs.⁷ Another strategy focuses on exploring ligands with different functional groups⁸ and connectors,⁹ or varying metal atoms from a single component such as Ni,¹⁰ Co,¹¹ Cu,¹² to bi- and tri-metal components.^{13,14} In principle, a more attractive and promising approach would be to reconstruct the original structures of MOFs towards the target structures by design, which holds a great potential to break through the performance bottleneck to

reach new heights in the OER activity and operating durability. In fact, an optimum OER catalyst in itself should be dynamically adaptable, thus naturally involves restructuring throughout the process. However, until now, such a strategy is yet to be explored.

Herein, we report the first successful molecular reconstruction of the interior frameworks of MOFs by a simple *in-situ* solvothermal modulation procedure, and the demonstration of the underlying mechanism for their high OER performance. MOF-74-Fe was used as the prototype with hexagonal channels and coordinated phenolic hydroxyl groups, and its modulated form MIL-53(Fe)-2OH was rationally designed and fabricated with rhombic channels and uncoordinated phenolic hydroxyl groups (**Figure 1a**). Density functional theory (DFT) calculations have revealed the highly reduced e_g-t_{2g} crystal field splitting in Fe-3d of MIL-53(Fe)-2OH, where the fast electron transfer pathways are mediated by the omnipresent molecularly assembled O sites. Leveraging on the desirable electronic structure, the modulated MIL-53(Fe)-2OH with uncoordinated phenolic hydroxyls exhibits unprecedentedly high intrinsic OER activity with a turnover frequency per metal site of 1.44 s^{-1} at 1.53 V vs. RHE, which is 81 times higher than that of the commercial IrO_2 catalyst. Moreover, the overpotentials of the MIL-53(Fe)-2OH catalyst are 215 and 314 mV at 10 mA cm^{-2} and 500 mA cm^{-2} , respectively, which are lower than those of the best MOF catalysts reported to date. Capitalizing on the MOF platform with molecular-level precision, this work is able not only to offer insightful understanding of the structure-property relationship but also to provide an innovative design strategy for systematically optimizing MOF-based electrocatalysts for OER and other important but challenging reactions.

Results And Discussion

Inspired by the promise of the rational design presented above, MIL-53(Fe)-2OH and MOF-74-Fe catalysts were synthesized by using 2,5-dihydroxyterephthalic acid (H_4DOBDC) as ligand and iron as the metal component. Synthesis of MOFs involves solid-to-solid rearrangement and intermediate formation.¹⁵⁻¹⁷ As shown in **Figure 1a** and **Figure S1**, H_4DOBDC have two carboxylic groups rigidly located at an angle of 180° (1,4-benzenedicarboxylic acid functionalities) and two phenolic functional groups.^{18,19} Deprotonation of H_4DOBDC can form two kinds of ligand anions: 2,5-dihydroxyterephthalato anion ($[\text{H}_2\text{DOBDC}]^{2-}$) with the pKa value of 7.31 and 2,5-dioxidoterephthalato tetra-anion ($[\text{DOBDC}]^{4-}$) with the pKa value of 26.67.^{20,21} Alkaline environment can be formed spontaneously through the solvothermal decomposition, even if base is absent from the starting reagents.¹⁵ The quadridentate ligand $[\text{DOBDC}]^{4-}$ can be easily formed, which tends to be incorporated into MOF-74-Fe (**Figure S2**).¹⁵ By controlling the solvent ratio and concentration, H_4DOBDC can be selectively deprotonated at only the two carboxylic groups, and consequently form the bidentate anion $[\text{H}_2\text{DOBDC}]^{2-}$, which leads to the formation of MIL-53(Fe)-2OH (**Figure S3**).²² Meanwhile, DFT calculations have also revealed the distinctly different electronic structures of these two MOFs. From the electronic distributions near the Fermi level (E_F), it is evident that the bonding orbitals in MOF-74-Fe are dominated by the carbon chains with only limited contributions from the Fe sites, leading to the relatively weak electroactivity of Fe (**Figure 1b**). In MIL-

MIL-53(Fe)-2OH, however, Fe sites display the highly electron-rich feature, indicating high electroactivity (**Figure 1c**). Meanwhile, O sites of the phenolic groups and the connection points also facilitate the electron transfer within MIL-53(Fe)-2OH for improved OER performance. The highly distinct electronic structures will lead to the different OER performances in these two MOFs. The projected partial density of states (PDOSs) in **Figure 1d** further reveals the distinct electronic structures. Notably, Fe-3d orbitals show a large e_g-t_{2g} splitting of 3.43 eV, leading to the large barriers for electron transfer in MOF-74-Fe. OH-s,p orbitals locate in the deep position, which mainly serves as the electron reservoir, and the resulting limited overlap between Fe-3d and OH-s,p orbitals increases the difficulties of site-to-site electron transfer. In contrast, the e_g-t_{2g} splitting of Fe-3d orbitals has been significantly alleviated to 1.19 eV in MIL-53(Fe)-2OH, which supports much more efficient electron transfer from the MOF to the intermediates (**Figure 1e**). C-s,p orbitals cover a broad range in both MOFs to facilitate electron depletion. More importantly, two different types of O sites have synergistically improved the OER performance. The O-s,p orbitals from Fe-O-Fe chains have shown a close position towards the E_F with good overlap with both Fe-3d and OH-s,p orbitals, indicating that the phenolic groups in MIL-53(Fe)-2OH are able to ensure the fast site-to-site electron transfer.

The crystal structures of the MIL-53(Fe)-2OH and MOF-74-Fe catalysts were investigated by X-ray powder diffraction (XRD). The experimental XRD pattern of the MIL-53(Fe)-2OH sample matches well with the MIL-53(Fe) structure (CCDC No. 734218) in the *Imma* space group with the unit cell parameters of $a = 17.84 \text{ \AA}$, $b = 6.87 \text{ \AA}$, $c = 11.84 \text{ \AA}$ and good agreement factors of weight-profile R -factor $R_{wp} = 7.3\%$ and underweighted R -factor $R_p = 5.6\%$ (**Figure 2a**). Moreover, the XRD pattern of the MOF-74-Fe sample conforms to the MOF-74 structure (CCDC No. 1494751, space group of *R-3*) with the unit cell parameters of $a = 26.13 \text{ \AA}$, $b = 26.13 \text{ \AA}$, $c = 6.72 \text{ \AA}$ (**Figure 2b**). Simulated XRD patterns are consistent with the experimental profiles of MIL-53(Fe)-2OH and MOF-74-Fe, suggesting the successful formation of the MIL-53(Fe) and MOF-74 structure.²³ The Raman spectra reveal the skeleton phonon modes of the carboxylate, phenolate, and benzene rings, and Fe-O in the obtained MOFs (**Figure S4**).²⁴ The four vibrational peaks appeared at ca. 1606, 1397, 1535, and 1302 cm^{-1} for the MIL-53(Fe)-2OH are ascribed to the in- and out-of-phase stretching region of the carboxylate group, $\nu(\text{COO}^-)$ vibration, and $\nu(\text{C-O})$ vibration, respectively.²⁴⁻²⁶ The peaks at 600 and 404 cm^{-1} are assigned to C-H stretching region of the benzene ring and Fe-O bonds vibration, respectively.^{24,26} By Raman spectroscopy analysis, although MIL-53(Fe)-2OH and MOF-74-Fe have similar coordinated structures, the vibration of hydroxyl group, C-O stretching vibration of the hydroxyl groups, carboxyl groups and Fe-O bond vibration are obviously different, indicating that the coordination environments are distinct in these two MOFs. Furthermore, Fourier transform infrared (FT-IR) spectroscopy was also employed to confirm the formation of MOFs (**Figure S5**). The 1211 cm^{-1} peak of MIL-53(Fe)-2OH is assigned to the C-O stretching vibration of the hydroxyl groups.^{27,28} The coordinated hydroxyl groups in MOF-74-Fe are difficult to form hydrogen bonds, resulting in the absorption peak moving to lower frequency.²⁹ Therefore, the C-O stretching vibration peak of MOF-74-Fe shifts to 1192 cm^{-1} . Importantly, the absorption peak at 3404 cm^{-1} for MIL-53(Fe)-2OH, which is absent for MOF-74-Fe, is related to the variation of phenolic hydroxyl group (νOH),

suggesting the successful fabrication of the two target MOF structures.^{30,31} The XPS survey spectrum for MIL-53(Fe)-2OH reveals the presence of C (62.4 at.%), O (34.3 at.%), Fe (3.3 at.%) (**Figure S6** and **Table S1**). High-resolution C 1s XPS spectra confirm the composition of the C=C/C-C in aromatic rings (284.7 eV), the C-O (286.4 eV), and the carboxylate group (O=C-O, 288.8 eV) for both the MIL-53(Fe)-2OH and MOF-74-Fe samples (**Figure S7**).^{8,32} The O 1s XPS spectrum of MOF-74-Fe can be deconvoluted into three energy peaks at 530.8 eV, 531.9 eV, and 533.7 eV, which are ascribed to the Fe-O bonds, the carboxylate of the organic ligands, and absorbed water, respectively (**Figure S8**).³² The O 1s XPS peak at 532.8 eV for MIL-53(Fe)-2OH is assigned to C-OH bonds. The fitting data showed that the content ratio of the Fe-O bond in MOF-74-Fe was slightly higher than that of MIL-53(Fe)-2OH, presumably related to the different coordination environments of the Fe ions with phenolic hydroxyl and carboxyl groups. The high-resolution XPS spectrum of MIL-53(Fe)-2OH at Fe 2p can be deconvoluted into four characteristic peaks shown in **Figure S9**, which are assigned to Fe³⁺ (712.4 eV and 725.6 eV) and associated shakeup satellites (716.6 eV and 730.3 eV), respectively.^{33,34}

X-ray absorption spectroscopy (XAS) was performed to further elucidate the fine structure of the synthesized MOFs. As shown in the X-ray absorption near-edge spectra (XANES) (**Figure 2c**), the Fe K-edge position of MIL-53(Fe)-2OH and MOF-74-Fe are close to that of Fe₂O₃. According to the linear fitting of the K-edge energy position of XANES spectra, the oxidation states of Fe in MIL-53(Fe)-2OH and MOF-74-Fe are +3.3 and +2.8, respectively (**Figure S10**), reflecting the effect of phenolic coordination. The fitting results of the Fe K-edge EXAFS spectra (**Table S3**) exhibit a higher Fe-O coordination number of MIL-53(Fe)-2OH (6.67) than that of MOF-74-Fe (6.28) in the first shell, which is perhaps related to the higher oxidation state of Fe in MIL-53(Fe)-2OH. The lowest intensity of the pre-edge peak at ≈ 7114 eV appears in MIL-53(Fe)-2OH, indicating the excellent symmetric octahedra [FeO₆] structure in MIL-53(Fe)-2OH, which is in good agreement with the simulated MIL-53(Fe) structure (CCDC: 734218) shown in Figure 2a and Figure S3. The pre-edge peak intensity of MOF-74-Fe is slightly higher, indicating the slightly lowered symmetry of the coordination sites. The coordination environment of Fe in MIL-53(Fe)-2OH is actually quite different from that of MOF-74-Fe.^{35,36} This effectively suggests that the different oxygenic coordination environment alters the local electron density of the metal sites and thus impact the catalytic activity.³⁷ The Fourier transform of the extended XAFS (EXAFS) spectra at the Fe K-edge and the corresponding fitting results are summarized in **Figure 2d** and **Figure S11-12**. The main peak of Fourier transforms (FTs) curves for MIL-53(Fe)-2OH (1.59 Å) and MOF-74-Fe (1.64 Å) correspond to the nearest Fe-O coordination, with no indication of the formation of Fe-Fe bond.³⁸ The signal of wavelet transforms (WT) for the k³-weighted Fe K-edge EXAFS curves related to Fe-Fe bonds has been detected in the Fe foil but not in MIL-53(Fe)-2OH and MOF-74-Fe, giving a strong indication that there are only atomically dispersed Fe sites in the MOF samples (**Figure 2e**). The maximum intensity signal at ~ 5.1 Å⁻¹ for MIL-53(Fe)-2OH is related to the Fe-O bond, which exhibits a positive shift in contrast to that of MOF-74-Fe (~ 4.75 Å⁻¹), indicating the different electronic structure between them. The Fe K-edge EXAFS data reveal a Fe-O bond length of 1.976 ± 0.04 Å and the Fe-O-C bond length of 3.179 ± 0.008 Å for MIL-53(Fe)-2OH, which show great consistency with the simulated structure based on the XRD analysis

(**Table S3** and **Figure S13**). Of note, the Fe–O bond length of MOF-74-Fe is slightly longer (1.996 ± 0.045 Å) than that of MIL-53(Fe)-2OH, and tallies with its lower oxidation state, which is also very much consonant with the XRD analysis (**Figure S14**). The different electronic structures of MIL-53(Fe)-2OH from MOF-74-Fe optimize the adsorption/desorption ability of oxygenic intermediates (OH^* , OOH^* , O^*) and thus improves the catalytic OER activity.^{24,39}

N_2 adsorption-desorption isotherms reveal that the Brunauer-Emmett-Teller (BET) surface of MIL-53(Fe)-2OH is $7.3 \text{ m}^2 \text{ g}^{-1}$, which is lower than that of the MOF-74-Fe ($10.4 \text{ m}^2 \text{ g}^{-1}$) (**Figure S15**). These two Fe-based MOFs catalysts exhibit an obvious adsorption hysteresis loop with typical IV-type isotherms, implying the mesoporous character. The measured pore sizes of MIL-53(Fe)-2OH and MOF-74-Fe are mainly concentrated at 1.48 nm and 1.59 nm, respectively, which are in good agreement with their crystal structure (**Figure 3a,b**). The morphologies of MIL-53(Fe)-2OH and MOF-74-Fe samples were examined by scanning electron microscopy (SEM) and transmission electron microscopy (TEM). As shown in **Figure 3c** and **Figure S16-17**, MIL-53(Fe)-2OH exhibits a regular octahedral structure. SEM image and corresponding energy dispersion spectrum (EDS) elemental mappings of MIL-53(Fe)-2OH are shown in **Figure 3d**. Apparently, the Fe, C, and O elements were distributed over the whole surface. The elemental mapping demonstrates the uniform distribution of Fe, C, and O elements in MIL-53(Fe)-2OH. In comparison, MOF-74-Fe exhibits polyhedral prism morphology with a width of 0.5-1 μm and a length of 10-25 μm (**Figure 3e** and **Figure S18**). The MOF-74-Fe prism self-assembles into micro-flowers. TEM images reveal that MOF-74-Fe is indeed composed of nanorods (**Figure S19**). As examined by SEM-EDS, the elemental mapping demonstrates the uniform distribution of Fe, C, and O elements in MOF-74-Fe (**Figure 3f** and **Table S2**). The electrocatalytic OER performances of MIL-53(Fe)-2OH and MOF-74-Fe samples were studied in a three-electrode system in the O_2 -saturated 1.0 M KOH solution at room temperature. According to the polarization curves shown in **Figure 4a**, the MIL-53(Fe)-2OH catalyst exhibits the lowest overpotential of 215 mV at a current density of 10 mA cm^{-2} , compared to that of the MOF-74-Fe (242 mV), and IrO_2 (335 mV) catalysts. The Tafel slope of the MIL-53(Fe)-2OH catalyst (45.4 mV dec^{-1}) is also lower than that of MOF-74-Fe (49.5 mV dec^{-1}), IrO_2 (99.7 mV dec^{-1}), and NF ($108.2 \text{ mV dec}^{-1}$) (**Figure 4b**, **Figure S20** and **Table S4**). The electrochemical active surface area (ECSAs) of the electrocatalyst is proportional to the electrochemical double-layer capacitance (C_{dl}), which can be determined by measuring the scanning rate-dependent cyclic voltammetry (CV) of the non-Faraday region (**Figures S21**). The measured C_{dl} value of MIL-53(Fe)-2OH is 4.2 mF cm^{-2} , which is closed to that of the MOF-74-Fe (4.1 mF cm^{-2}) and larger than that of IrO_2 (3.0 mF cm^{-2}) (**Figure S22**).

As calculated from geometric current densities and ECSAs, the highest specific current density (j_{ECSA}) is achieved over MIL-53(Fe)-2OH (3.24 mA cm^{-2}), which is much higher than that of MOF-74-Fe (1.42 mA cm^{-2}) and IrO_2 (0.08 mA cm^{-2}) catalysts, indicating its superior intrinsic activity for OER (**Figures S23**). To further illustrate the electrode reaction kinetics during the catalytic OER process, electrochemical impedance spectroscopy (EIS) was performed. As shown in **Figure 4c**, the Nyquist plots reveal that MIL-53(Fe)-2OH has an ultra-low charge transfer resistance (R_{ct}) of about 0.65Ω at the overpotential of 300

mV (at 1.53 V vs. RHE) in alkaline condition, which is lower than that of the MOF-74-Fe (0.80 Ω) and IrO₂ (18.32 Ω) catalysts, indicating a much faster charge transfer on the MIL-53(Fe)-2OH surface in the electrochemical reaction process. These results firmly demonstrated the excellent activity of MIL-53(Fe)-2OH for OER. In addition, the turnover frequency (TOF) and the mass activity (MA) of the catalysts were also determined to illustrate the intrinsic activity at the constant overpotential of 300 mV (**Figure 4d**).^{24,40} More details of the kinetic model have been presented in section 1.4 and 1.5 of the Supplementary Information. The high TOF of 1.44 s⁻¹ is obtained for the MIL-53(Fe)-2OH catalyst, prominently exceeding that of MOF-74-Fe (0.59 s⁻¹) and IrO₂ (0.0177 s⁻¹) (**Figure S24**). The MA value of MIL-53(Fe)-2OH could reach as high as 357.90 A g⁻¹, significantly larger than those of MOF-74-Fe (153.60 A g⁻¹) and IrO₂ (62.34 A g⁻¹) (**Figure S25** and **Table S5**). Taken together, these results clearly indicate that the MIL-53(Fe)-2OH exhibits exceptional catalytic OER activities in terms of the lower Tafel slope and lower overpotential, which exceeds most of the recently reported MOFs OER catalysts, as shown in **Figure 4e** and **Table S6**.^{4,14,25,34,41-52}

The OER performances of MOF-74-Fe and MIL-53(Fe)-2OH have further been elucidated by DFT calculations from both electronic structures and reaction energy. In MOF-74-Fe, the size of e_g-t_{2g} splitting increases with the coordination numbers (**Figure 5a**). The existence of OH vacancy also cannot evidently lower the e_g-t_{2g} splitting, demonstrating that electron transfer in Fe sites of MOF-74-Fe is lowered due to the large barriers. For different types of C sites within MOF-74-Fe, most carbon sites displayed low p-band centers, which demonstrated their limited contributions to the electron transfer during OER (**Figure S26**). For MIL-53(Fe)-2OH, the carbon sites in the benzene ring are more electroactive than that in O-C-O and the formation of OH vacancy further improves the electron transfer (**Figure 5b**). This indicates that the existence of the electroactive phenolic groups is able to not only facilitate the electron transfer but also improve the overall electroactivity. Since the electronic structures are highly correlated with the OER performances, the PDOSs of key intermediates on both MOFs are demonstrated (**Figure 5c-d**). For MOF-74-Fe, it is noted that the upshifting trend of the σ orbitals from O-species has shown an evident deviation at OOH*, which potentially increases the barriers for the conversion from O* to OOH*. Meanwhile, such a deviation is absent in MIL-53(Fe)-2OH, which achieves the efficient conversions of intermediates with low energy barriers. These results further confirm that the superior OER performances of MIL-53(Fe)-2OH originate from the optimal electronic structures modulated by the phenolic groups. The loss of OH groups in both MOFs shows high energy costs of 3.34 eV and 2.65 eV in MOF-74-Fe and MIL-53(Fe)-2OH, respectively (**Figure S27**). This illustrates that the involvement of OH groups from MOF to promote the OER is challenging. More importantly, this further reveals that the more electroactive Fe and O sites in MIL-53(Fe)-2OH are the key factors for the highly efficient OER process. The reaction energy

change of OER has been compared between the two MOFs. With $U = 0$ V, both MOFs display the largest energy cost at the conversion from O^* to OOH^* as the rate-determining step (**Figure S28**). The energy barrier in MIL-53(Fe)-2OH is smaller than that of the MOF-74-Fe, which is consistent with the results of electronic structures. After introducing the equilibrium potential, we notice that the improved OER performances of MIL-53(Fe)-2OH are attributed to suitable binding of OH^* , which results in a reduced energy barrier of 0.23 eV than that of the 0.32 eV in MOF-74-Fe (**Figure 5e** and **Figure S29**). On the other side, the over-binding of OH^* leads to a continuous uphill trend in MOF-74-Fe, which has affected the efficiency of the OER process. The reaction mechanism of OER has been

demonstrated through the structural configurations (**Figure S30-31**). Notably, the frameworks of MOF are able to remain relatively stable during the adsorption of the intermediates. Moreover, the selectivity between $2e^-$ and $4e^-$ OER have been compared based on the conversion reaction of O^* . For both MOF-74-Fe and MIL-53(Fe)-2OH, the $4e^-$ OER is more preferred due to the much smaller energy barrier of $O^* \rightarrow OOH^*$ than $O^* \rightarrow \frac{1}{2} O_2$, indicating the high selectivity towards $4e^-$ OER.

The chronopotentiometry responses (E-t) curve in **Figure 6a** demonstrates that the as-synthesized MIL-53(Fe)-2OH and MOF-74-Fe catalysts possess good durability after the OER test for more than 100 hours at 100 mA cm^{-2} . The polarization curves of the MIL-53(Fe)-2OH and MOF-74-Fe catalysts after the stability test have no obvious changes of the overpotential before and after the chronopotentiometry test at the high current density of 100 mA cm^{-2} (**Figure S32**). The overpotential of MIL-53(Fe)-2OH after 100 h of the stability test increases only 2 mV at the current density of 100 mA cm^{-2} , which suggests that the MIL-53(Fe)-2OH exhibits excellent long-term stability (**Figure 6b**). The overpotential after the stability test increases 10 mV at the current density of 100 mA cm^{-2} for MOF-74-Fe catalyst (**Figure S33-34**). C_{dl} values of the MIL-53(Fe)-2OH (3.8 mF cm^{-2}), MOF-74-Fe (3.9 mF cm^{-2}) and IrO_2 (2.9 mF cm^{-2}) catalysts exhibit no obvious changes comparing to their initial ones (**Figure S35-37**). The overpotential at the current density of 100 mA cm^{-2} for MIL-53(Fe)-2OH after 100 hours of stability test (266.8 mV) only increases 0.6 mV compared to the initial value (266.2 mV), which is much lower than that of MOF-74-Fe (5.9 mV) and IrO_2 (32.4 mV). Compared with MOF-74-Fe and IrO_2 , the R_{ct} value of MIL-53(Fe)-2OH also show the minimum increase after the stability test (0.26 Ω) compared to MOF-74-Fe (0.80 Ω) and IrO_2 (21.1 Ω) at the overpotential of 300 mV, confirming the superior electrochemical durability of the MIL-53(Fe)-2OH catalyst (**Figure 6c** and **Figure S38-40**).

Furthermore, XRD, XPS, TEM and SEM were performed to probe the essential difference in the catalysts' structure during the OER process. As shown in **Figure S41-42**, the XRD patterns of MIL-53(Fe)-2OH and MOF-74-Fe after the OER stability test agree well with that of $FeO(OH)$ (ICSD No. 94874), which demonstrates the formation of iron hydroxides.⁵³ The structure and electronic properties of MIL-53(Fe)-2OH after stability test was further analyzed by XPS. The XPS analysis discloses the presence of Fe (4.3 at.%), C (36.5 at.%) and O (59.2 at.%) elements in MIL-53(Fe)-2OH catalysts after OER for 100 h, in

which O content was significantly higher than that of the initial MIL-53(Fe)-2OH (**Table S1**). As shown in **Figure S43a**, the high-resolution XPS spectrum of Fe 2p shows deconvoluted peaks for Fe³⁺ (711.9 eV, 725.8 eV).^{27,54,55} The O 1s spectrum can be split into three peaks at 530.7, 532.8, and 534.1 eV, which are ascribed to the Fe–O, C–OH, and adsorbed water, respectively (**Figure S43b**).^{56,57} These results suggest a structural transformation of the MIL-53(Fe)-2OH catalyst.^{26,27,58} MIL-53(Fe)-2OH catalyst (**Figure S46**). The HRTEM image of MIL-53(Fe)-2OH displays the lattice fringes with the interlayer distance of 0.29 nm, which correspond to the (220) planes of FeO(OH) (**Figure S46c**). It can be known from **Figure S47** that the C, O, and Fe elements are spread over the whole region for the MIL-53(Fe)-2OH catalyst after for 100 h OER stability test at 100 mA cm⁻². The morphology of MIL-53(Fe)-2OH and MOF-74-Fe after stability test was observed by SEM and TEM. As shown in **Figure S44**, the MIL-53(Fe)-2OH is transformed from the original regular octahedral structure to the morphology of bulk stacking. For MOF-74-Fe, the polyhedral prism morphology is transformed into sheets (**Figure S45**). TEM analysis further confirmed the phase transition of the

The structure-property dependency of the MIL-53(Fe)-2OH catalyst during the OER process was further investigated by the real-time kinetic simulation. Following the procedure of our previous work,^{59,60} the standard activation free energies for the five elementary reaction steps (for the oxidative adsorption step, for the first oxidative transition step, for the associative desorption step, for the second oxidative transition step and for the oxidative desorption step) and the standard free energy for intermediate adsorption (, for OH*, for O* and for OOH*) of OER process were evaluated by building the OER kinetic model and then best-fitting ($R^2 = 0.999$) the kinetic current density of MIL-53(Fe)-2OH (**Figure 6d-e**). More details of the kinetic model are presented in section 1.7 of the Supplementary Information. It can be seen in **Figure S48-49** that the free energy for the associative desorption step () is much higher than that for the second oxidative transition step () and the formation of OOH* (), indicating that the 4e⁻ pathway dominates the OER process on the MIL-53(Fe)-2OH catalyst system, in good agreement with the DFT calculations. The free energy diagram shown in **Figure 5f** indicates the formation of the reaction intermediate OOH* from the adsorbed O* is the rate-determining step on the MIL-53(Fe)-2OH surface, which is in good agreement with the DFT calculations. **Figure 6e** shows the adsorption isotherms of the reaction intermediates. The fractional coverages of the intermediates, , and , are closely correlated to their standard free energy. The low accelerates the formation and adsorption of O*, leading to the high coverage of O* on the MIL-53(Fe)-2OH surface. In the higher overpotential range, the consumption rate of O* to form OOH* increases, resulting in the decrease of and the increase of the fractional coverage of OOH*. The strong adsorption of the intermediates on the MIL-53(Fe)-2OH surface promotes the generation of the FeO(OH) phase during the OER process. It is worth noting from **Figure 6f** that the activation energies for the rate-determining step are very close on the initial and post-tested MIL-53(Fe)-2OH catalyst, confirming the robustness of the catalyst with an invariant OER activity even after the long-term OER operational testing.

Although MIL-53(Fe)-2OH catalyst exhibits excellent OER stability within the testing time interval, the chemical structure of the MIL-53(Fe)-2OH catalyst has changed after the OER stability testing, so

its kinetic behavior and intermediate coverages may also change after the OER stability test. Indeed, the OER kinetics of the post-tested MIL-53(Fe)-2OH catalyst is dependent on both the formation of OOH^* and the adsorption of OH^* with an increased energy barrier of 280 meV compared to the initial one (171 meV) (**Figure 6f**). Because of the higher energy barrier for the formation of the first intermediate (OH^*), the fractional coverages of all the intermediates (OH^* , O^* , and OOH^*) on the post-tested MIL-53(Fe)-2OH surface are lower than those of the initial counterpart, confirming a changed kinetic behavior of the MIL-53(Fe)-2OH catalyst during the OER process (**Figure S50**). Thus the real-time kinetic simulation opens a new direction in exploring the OER mechanism and can help to develop robust OER electrocatalysts with competitive activity and stability.

Conclusions

In summary, this study has proposed and demonstrated a feasible synthesis strategy to rationally reconstruct the MOF structure from the phenolic hydroxyl coordinated MOF-74-Fe with hexagonal channels to uncoordinated MIL-53(Fe)-2OH with rhombic channels. XAS analyses and DFT calculations have revealed that the different electronic structures of Fe sites in MOF-74-Fe and MIL-53(Fe)-2OH due to the precisely tuned ligand fields, which further lead to the varied electroactivity towards the OER process. It is found that the much-reduced e_g-t_{2g} splitting of Fe-3d orbitals with electroactive O sites in the MIL-53(Fe)-2OH guarantees the efficient OER with lowered overpotential at the rate-determining step. Leveraging on the desirable electronic structure, the purpose-built MIL-53(Fe)-2OH catalyst delivers remarkably fast OER kinetics with low overpotential of 215 mV at 10 mA cm^{-2} , small Tafel slope of 45.4 mV dec^{-1} , competitive TOF value of 1.44 s^{-1} and mass activity of 153.60 A g^{-1} at the overpotential of 300 mV. Furthermore, the real-time kinetic simulation elucidates a pronouncedly changed kinetic behavior of MIL-53(Fe)-2OH during the OER process. By combining the advantages of homogeneous and heterogeneous catalysts, this work offers a novel design strategy based on the molecular MOF reconstruction with delicate modulations of coordination environments and electronic structures of active sites, which will open a new direction for the future development of efficient OER electrocatalysts.

Methods

Synthesis of hydroxyl functionalized metal-organic framework MIL-53(Fe)-2OH

First, H_4DOBDC (0.20 g) and $\text{FeCl}_3 \cdot 6\text{H}_2\text{O}$ (0.27 g) were dissolved in DMF (12 mL). Ultrasonicated for 5 min and then the uniform mixture was transferred into a 50 mL Teflon-lined stainless-steel autoclave and heated for 24 hours at $110 \text{ }^\circ\text{C}$. Cooling it to room temperature, it is filtered by a microporous filter membrane and washed with EtOH and DI water three-time. Finally, the MIL-53(Fe)-2OH is dried in a drying oven at $50 \text{ }^\circ\text{C}$ for 12 hours.

Synthesis of Fe-Metal-Organic Frameworks-74 (MOF-74-Fe)

Fe-Metal-Organic Frameworks-74 (MOF-74-Fe) was prepared according to literature reports.³⁴ Typically, $\text{FeCl}_2 \cdot 4\text{H}_2\text{O}$ (0.10 g) and H_4DOBDC (0.22 g) were dissolved in 7.5 mL DMF-EtOH-water mixture (1:1:1 (v/v/v)) under magnetic stirring at room temperature to form a mixture solution. The obtained mixture solution was transferred into a 50 mL Teflon-lined stainless-steel autoclave to heat at 120 °C for 24 hours. The powder was collected by washing/filtered with EtOH and DMF several times to remove organic residues and dried at 100 °C for overnight.

Declarations

Competing interests

The authors declare no competing interests.

Acknowledgements

This research is supported by the National Nature Science Foundation of China (Nos. 21862011, 51864024, 21972006), National Key R&D Program of China (2021YFA1501101), the National Natural Science Foundation of China/RGC Joint Research Scheme (N_PolyU502/21), and the funding for Projects of Strategic Importance of The Hong Kong Polytechnic University (Project Code: 1-ZE2V), and Shenzhen Peacock Plan (KQTD2016053015544057).

Author contributions

C.Z., J.H. and L.Z. developed the idea and designed the experiments. C.Z. and Q.Q. synthesized the catalyst and performed electrochemical experiments. C.Z. and Q.Q. characterized the morphology and chemical structure of the catalysts. M. S. and B.H. performed the theoretical calculations along with structure modeling and simulations. J.H. and C.Z. performed the real-time kinetic simulation. Y.M. and J.H. carried out the XAS measurements and analyses. J.H., B.H., C.Z., Q.Q. and S.Y. wrote the manuscript. J.H., B.H., L.Z. and S.Y. supervised the project. All authors discussed the results and assisted during manuscript preparation.

References

1. Guo, J., Zhang, Y., Zhu, Y., Long, C., Zhao, M., He, M., Zhang, X., Lv, J., Han, B. & Tang, Z. Ultrathin chiral metal–organic-framework nanosheets for efficient enantioselective separation. *Angew. Chem. Int. Ed.* **57**, 6873–6877, (2018).
2. Qi, Q., Hu, J., Zhang, Y., Li, W., Huang, B. & Zhang, C. Two-Dimensional Metal–Organic Frameworks-Based Electrocatalysts for Oxygen Evolution and Oxygen Reduction Reactions. *Adv. Energy Sustainability Res.* **2**, 2000067, (2021).
3. Meng, C., Ling, T., Ma, T.-Y., Wang, H., Hu, Z., Zhou, Y., Mao, J., Du, X.-W., Jaroniec, M. & Qiao, S.-Z. Atomically and electronically coupled Pt and CoO hybrid nanocatalysts for enhanced electrocatalytic performance. *Adv. Mater.* **29**, 1604607, (2017).

- Huang, J., Li, Y., Huang, R.-K., He, C.-T., Gong, L., Hu, Q., Wang, L., Xu, Y.-T., Tian, X.-Y., Liu, S.-Y., Ye, Z.-M., Wang, F., Zhou, D.-D., Zhang, W.-X. & Zhang, J.-P. Electrochemical exfoliation of pillared-layer metal-organic framework to boost the oxygen evolution reaction. *Angew. Chem. Int. Ed.* **57**, 4632–4636, (2018).
- Zhao, S., Wang, Y., Dong, J., He, C.-T., Yin, H., An, P., Zhao, K., Zhang, X., Gao, C., Zhang, L., Lv, J., Wang, J., Zhang, J., Khattak, A. M., Khan, N. A., Wei, Z., Zhang, J., Liu, S., Zhao, H. & Tang, Z. Ultrathin metal-organic framework nanosheets for electrocatalytic oxygen evolution. *Nat. Energy* **1**, 16184 (2016).
- Yuan, Q., Yu, Y., Gong, Y. & Bi, X. Three-dimensional N-doped carbon nanotube frameworks on Ni foam derived from a metal-organic framework as a bifunctional electrocatalyst for overall water splitting. *ACS Appl. Mater. Interfaces* **12**, 3592–3602, (2020).
- Xue, Z., Liu, K., Liu, Q., Li, Y., Li, M., Su, C.-Y., Ogiwara, N., Kobayashi, H., Kitagawa, H., Liu, M. & Li, G. Missing-linker metal-organic frameworks for oxygen evolution reaction. *Nat. Commun.* **10**, 5048, (2019).
- Qi, Q., Tai, J., Hu, J., Zhang, Z., Dai, L., Song, H., Shao, M., Zhang, C. & Zhang, L. Ligand functionalized iron-based metal-organic frameworks for efficient electrocatalytic oxygen evolution. *ChemCatChem* **13**, 4976–4984, (2021).
- Lin, Y., Wan, H., Wu, D., Chen, G., Zhang, N., Liu, X., Li, J., Cao, Y., Qiu, G. & Ma, R. Metal-organic framework hexagonal nanoplates: bottom-up synthesis, topotactic transformation, and efficient oxygen evolution reaction. *J. Am. Chem. Soc.* **142**, 7317–7321, (2020).
- Hu, Q., Huang, X., Wang, Z., Li, G., Han, Z., Yang, H., Ren, X., Zhang, Q., Liu, J. & He, C. Unconventionally fabricating defect-rich NiO nanoparticles within ultrathin metal-organic framework nanosheets to enable high-output oxygen evolution. *J. Mater. Chem. A* **8**, 2140–2146, (2020).
- Xu, Y., Li, B., Zheng, S., Wu, P., Zhan, J., Xue, H., Xu, Q. & Pang, H. Ultrathin two-dimensional cobalt-organic framework nanosheets for high-performance electrocatalytic oxygen evolution. *J. Mater. Chem. A* **6**, 22070–22076, (2018).
- Zhou, J., Dou, Y., Zhou, A., Shu, L., Chen, Y. & Li, J.-R. Layered metal-organic framework-derived metal oxide/carbon nanosheet arrays for catalyzing the oxygen evolution reaction. *ACS Energy Lett.* **3**, 1655–1661, (2018).
- Wei, X., Li, N. & Liu, N. Ultrathin NiFeZn-MOF nanosheets containing few metal oxide nanoparticles grown on nickel foam for efficient oxygen evolution reaction of electrocatalytic water splitting. *Electrochim. Acta* **318**, 957–965, (2019).
- Qi, Q., Hu, J., Guo, S., Song, H., Wang, S., Yao, Y., Le, T., Li, W., Zhang, C. & Zhang, L. Large-scale synthesis of low-cost bimetallic polyphthalocyanine for highly stable water oxidation. *Appl. Catal. B: Environ.* **299**, 120637, (2021).
- Du Bois, D. R., Wright, K. R., Bellas, M. K., Wiesner, N. & Matzger, A. J. Linker deprotonation and structural evolution on the pathway to MOF-74. *Inorg. Chem.* **61**, 4550–4554, (2022).

16. Xing, J., Schweighauser, L., Okada, S., Harano, K. & Nakamura, E. Atomistic structures and dynamics of prenucleation clusters in MOF-2 and MOF-5 syntheses. *Nat. Commun.* **10**, 3608, (2019).
17. Embrechts, H., Kriesten, M., Ermer, M., Peukert, W., Hartmann, M. & Distaso, M. In situ Raman and FTIR spectroscopic study on the formation of the isomers MIL-68(Al) and MIL-53(Al). *RSC Adv.* **10**, 7336–7348, (2020).
18. Wang, Y.-L., Jiang, Y.-L., Xiahou, Z.-J., Fu, J.-H. & Liu, Q.-Y. Diversity of lanthanide(III)-2,5-dihydroxy-1,4-benzenedicarboxylate extended frameworks: syntheses, structures, and magnetic properties. *Dalton T.* **41**, 11428–11437, (2012).
19. De Bellis, J., Dell'Amico, D. B., Ciancaleoni, G., Labella, L., Marchetti, F. & Samaritani, S. Interconversion of lanthanide-organic frameworks based on the anions of 2, 5-dihydroxyterephthalic acid as connectors. *Inorg. Chim. Acta* **495**, 118937, (2019).
20. Lu, P., Wu, Y., Kang, H., Wei, H., Liu, H. & Fang, M. What can pKa and NBO charges of the ligands tell us about the water and thermal stability of metal organic frameworks? *J. Mater. Chem. A* **2**, 16250–16267, (2014).
21. Zhang, S., Baker, J. & Pulay, P. A reliable and efficient first principles-based method for predicting pKa values. 2. organic acids. *J. Phys. Chem. A* **114**, 432–442, (2010).
22. Kundu, T., Wahiduzzaman, M., Shah, B. B., Maurin, G. & Zhao, D. Solvent-induced control over breathing behavior in flexible metal–organic frameworks for natural-gas delivery. *Angew. Chem. Int. Ed.* **58**, 8073–8077, (2019).
23. Devic, T., Horcajada, P., Serre, C., Salles, F., Maurin, G., Moulin, B., Heurtaux, D., Clet, G., Vimont, A., Grenèche, J.-M., Ouay, B. L., Moreau, F., Magnier, E., Filinchuk, Y., Marrot, J., Lavalley, J.-C., Daturi, M. & Férey, G. Functionalization in flexible porous solids: effects on the pore opening and the host – guest interactions. *J. Am. Chem. Soc.* **132**, 1127–1136, (2010).
24. Zhou, J., Han, Z., Wang, X., Gai, H., Chen, Z., Guo, T., Hou, X., Xu, L., Hu, X., Huang, M., Levchenko, S. V. & Jiang, H. Discovery of quantitative electronic structure-OER activity relationship in metal-organic framework electrocatalysts using an integrated theoretical-experimental approach. *Adv. Funct. Mater.* **31**, 2102066, (2021).
25. Sun, F., Wang, G., Ding, Y., Wang, C., Yuan, B. & Lin, Y. NiFe-based metal–organic framework nanosheets directly supported on nickel foam acting as robust electrodes for electrochemical oxygen evolution reaction. *Adv. Energy Mater.* **8**, 1800584, (2018).
26. Zha, Q., Li, M., Liu, Z. & Ni, Y. Hierarchical Co,Fe-MOF-74/Co/carbon cloth hybrid electrode: Simple construction and enhanced catalytic performance in full water splitting. *ACS Sustain. Chem. Eng.* **8**, 12025–12035, (2020).
27. Wang, Q., Wei, F., Manoj, D., Zhang, Z., Xiao, J., Zhao, X., Xiao, F., Wang, H. & Wang, S. In situ growth of Fe(II)-MOF-74 nanoarrays on nickel foam as an efficient electrocatalytic electrode for water oxidation: a mechanistic study on valence engineering. *Chem. Commun.* **55**, 11307–11310, (2019).
28. Xing, J., Guo, K., Zou, Z., Cai, M., Du, J. & Xu, C. In situ growth of well-ordered NiFe-MOF-74 on Ni foam by Fe²⁺ induction as an efficient and stable electrocatalyst for water oxidation. *Chem.*

- Commun. **54**, 7046–7049, (2018).
29. Chen, S., Liu, J., Xu, Y., Li, Z., Wang, T., Xu, J. & Wang, Z. Hydrogen storage properties of the novel crosslinked UiO-66-(OH)₂. *Int. J. Hydrogen Energy* **43**, 15370–15377, (2018).
30. Andonova, S., Ivanova, E., Yang, J. & Hadjiivanov, K. Adsorption forms of CO₂ on MIL-53(Al) and MIL-53(Al)-OH_x as revealed by FTIR spectroscopy. *J. Phys. Chem. C* **121**, 18665–18673, (2017).
31. Wang, J., Daignebonne, C., Suffren, Y., Freslon, S., Calvez, G., Bernot, K. & Guillou, O. New lanthanide-based coordination polymers with 2,5-dihydroxyterephthalate. *Inorg. Chim. Acta* **527**, 120594, (2021).
32. Wu, F., Guo, X., Wang, Q., Lu, S., Wang, J., Hu, Y., Hao, G., Li, Q., Yang, M.-Q. & Jiang, W. A hybrid of MIL-53(Fe) and conductive sulfide as a synergistic electrocatalyst for the oxygen evolution reaction. *J. Mater. Chem. A* **8**, 14574–14582, (2020).
33. Rodenas, T., Luz, I., Prieto, G., Seoane, B., Miro, H., Corma, A., Kapteijn, F., Llabrés i Xamena, F. X. & Gascon, J. Metal–organic framework nanosheets in polymer composite materials for gas separation. *Nat. Mater.* **14**, 48–55, (2015).
34. Zhao, X., Pattengale, B., Fan, D., Zou, Z., Zhao, Y., Du, J., Huang, J. & Xu, C. Mixed-node metal–organic frameworks as efficient electrocatalysts for oxygen evolution reaction. *ACS Energy Lett.* **3**, 2520–2526, (2018).
35. Zhang, L., Cai, W., Bao, N. & Yang, H. Implanting an Electron Donor to Enlarge the d–p Hybridization of High-Entropy (Oxy)hydroxide: A Novel Design to Boost Oxygen Evolution. *Adv. Mater.* **34**, 2110511, (2022).
36. Bai, L., Hsu, C.-S., Alexander, D. T. L., Chen, H. M. & Hu, X. Double-atom catalysts as a molecular platform for heterogeneous oxygen evolution electrocatalysis. *Nat. Energy* **6**, 1054–1066, (2021).
37. Wu, Y., Ding, Y., Han, X., Li, B., Wang, Y., Dong, S., Li, Q., Dou, S., Sun, J. & Sun, J. Modulating coordination environment of Fe single atoms for high-efficiency all-pH-tolerated H₂O₂ electrochemical production. *Appl. Catal. B: Environ.* **315**, 121578, (2022).
38. Luo, Y., Zhang, Z., Yang, F., Li, J., Liu, Z., Ren, W., Zhang, S. & Liu, B. Stabilized hydroxide-mediated nickel-based electrocatalysts for high-current-density hydrogen evolution in alkaline media. *Energy Environ. Sci.* **14**, 4610–4619, (2021).
39. Fei, B., Chen, Z., Liu, J., Xu, H., Yan, X., Qing, H., Chen, M. & Wu, R. Ultrathinning nickel sulfide with modulated electron density for efficient water splitting. *Adv. Energy Mater.* **10**, 2001963, (2020).
40. Li, W., Watzele, S., El-Sayed, H. A., Liang, Y., Kieslich, G., Bandarenka, A. S., Rodewald, K., Rieger, B. & Fischer, R. A. Unprecedented high oxygen evolution activity of electrocatalysts derived from surface-mounted metal–organic frameworks. *J. Am. Chem. Soc.* **141**, 5926–5933, (2019).
41. Yan, L., Cao, L., Dai, P., Gu, X., Liu, D., Li, L., Wang, Y. & Zhao, X. Metal-organic frameworks derived nanotube of nickel–cobalt bimetal phosphides as highly efficient electrocatalysts for overall water splitting. *Adv. Funct. Mater.* **27**, 1703455, (2017).
42. Wang, X., Xiao, H., Li, A., Li, Z., Liu, S., Zhang, Q., Gong, Y., Zheng, L., Zhu, Y., Chen, C., Wang, D., Peng, Q., Gu, L., Han, X., Li, J. & Li, Y. Constructing NiCo/Fe₃O₄ heteroparticles within MOF-74 for efficient

- oxygen evolution reactions. *J. Am. Chem. Soc.* **140**, 15336–15341, (2018).
43. Yan, L., Jiang, H., Xing, Y., Wang, Y., Liu, D., Gu, X., Dai, P., Li, L. & Zhao, X. Nickel metal–organic framework implanted on graphene and incubated to be ultrasmall nickel phosphide nanocrystals acts as a highly efficient water splitting electrocatalyst. *J. Mater. Chem. A* **6**, 1682–1691, (2018).
44. Zhuang, L., Ge, L., Liu, H., Jiang, Z., Jia, Y., Li, Z., Yang, D., Hocking, R. K., Li, M., Zhang, L., Wang, X., Yao, X. & Zhu, Z. A Surfactant-Free and Scalable General Strategy for Synthesizing Ultrathin Two-Dimensional Metal–Organic Framework Nanosheets for the Oxygen Evolution Reaction. *Angew. Chem. Int. Ed.* **58**, 13565–13572, (2019).
45. Wang, Q., Liu, Z., Zhao, H., Huang, H., Jiao, H. & Du, Y. MOF-derived porous Ni₂P nanosheets as novel bifunctional electrocatalysts for the hydrogen and oxygen evolution reactions. *J. Mater. Chem. A* **6**, 18720–18727, (2018).
46. He, P., Xie, Y., Dou, Y., Zhou, J., Zhou, A., Wei, X. & Li, J.-R. Partial sulfurization of a 2D MOF array for highly efficient oxygen evolution reaction. *ACS Appl. Mater. Inter.* **11**, 41595–41601, (2019).
47. Li, F.-L., Wang, P., Huang, X., Young, D. J., Wang, H.-F., Braunstein, P. & Lang, J.-P. Large-scale, bottom-up synthesis of binary metal–organic framework nanosheets for efficient water oxidation. *Angew. Chem. Int. Ed.* **58**, 7051–7056, (2019).
48. Xu, J., Zhu, X. & Jia, X. From low to high-crystallinity bimetal–organic framework nanosheet with highly exposed boundaries: An efficient and stable electrocatalyst for oxygen evolution reaction. *ACS Sustain. Chem. Eng.* **7**, 16629–16639, (2019).
49. Gao, Z., Yu, Z. W., Liu, F. Q., Yang, C., Yuan, Y. H., Yu, Y. & Luo, F. Stable Iron Hydroxide Nanosheets@Cobalt-Metal–Organic–Framework Heterostructure for Efficient Electrocatalytic Oxygen Evolution. *ChemSusChem* **12**, 4623–4628, (2019).
50. Gao, Z., Yu, Z. W., Liu, F. Q., Yu, Y., Su, X. M., Wang, L., Xu, Z. Z., Yang, Y. L., Wu, G. R., Feng, X. F. & Luo, F. Ultralow-Content Iron-Decorated Ni-MOF-74 Fabricated by a Metal–Organic Framework Surface Reaction for Efficient Electrocatalytic Water Oxidation. *Inorg. Chem.* **58**, 11500–11507, (2019).
51. Zhou, W., Xue, Z., Liu, Q., Li, Y., Hu, J. & Li, G. Trimetallic MOF-74 Films Grown on Ni Foam as Bifunctional Electrocatalysts for Overall Water Splitting. *ChemSusChem* **13**, 5647–5653, (2020).
52. Mu, X., Yuan, H., Jing, H., Xia, F., Wu, J., Gu, X., Chen, C., Bao, J., Liu, S. & Mu, S. Superior electrochemical water oxidation in vacancy defect-rich 1.5 nm ultrathin trimetal-organic framework nanosheets. *Appl. Catal. B: Environ.* **296**, 120095, (2021).
53. Morán, E., Blesa, M. C., Medina, M. E., Tornero, J. D., Menéndez, N. & Amador, U. Nonstoichiometric spinel ferrites obtained from α -NaFeO₂ via molten media reactions. *Inorg. Chem.* **41**, 5961–5967, (2002).
54. Zhao, S., Li, M., Han, M., Xu, D., Yang, J., Lin, Y., Shi, N.-E., Lu, Y., Yang, R., Liu, B., Dai, Z. & Bao, J. Defect-rich Ni₃FeN nanocrystals anchored on N-doped graphene for enhanced electrocatalytic oxygen evolution. *Adv. Funct. Mater.* **28**, 1706018, (2018).

55. Tang, C., Zhang, R., Lu, W., He, L., Jiang, X., Asiri, A. M. & Sun, X. Fe-doped CoP nanoarray: A monolithic multifunctional catalyst for highly efficient hydrogen generation. *Adv. Mater.* **29**, 1602441, (2017).
56. Wei, B., Shang, C., Wang, X. & Zhou, G. Conductive FeOOH as multifunctional interlayer for superior lithium–sulfur batteries. *Small* **16**, 2002789, (2020).
57. Zhang, E., Wang, B., Yu, X., Zhu, J., Wang, L. & Lu, B. β -FeOOH on carbon nanotubes as a cathode material for Na-ion batteries. *Energy Stor. Mater.* **8**, 147–152, (2017).
58. Zhao, S., Tan, C., He, C.-T., An, P., Xie, F., Jiang, S., Zhu, Y., Wu, K.-H., Zhang, B., Li, H., Zhang, J., Chen, Y., Liu, S., Dong, J. & Tang, Z. Structural transformation of highly active metal–organic framework electrocatalysts during the oxygen evolution reaction. *Nat. Energy* **5**, 881–890, (2020).
59. Hu, J., Zhang, C., Jiang, L., Lin, H., An, Y., Zhou, D., Leung, M. K. H. & Yang, S. Nanohybridization of MoS₂ with layered double hydroxides efficiently synergizes the hydrogen evolution in alkaline media. *Joule* **1**, 383–393, (2017).
60. Hu, J., Zhang, C., Yang, P., Xiao, J., Deng, T., Liu, Z., Huang, B., Leung, M. K. H. & Yang, S. Kinetic-oriented construction of MoS₂ synergistic interface to boost pH-universal hydrogen evolution. *Adv. Funct. Mater.* **30**, 1908520, (2020).

Figures

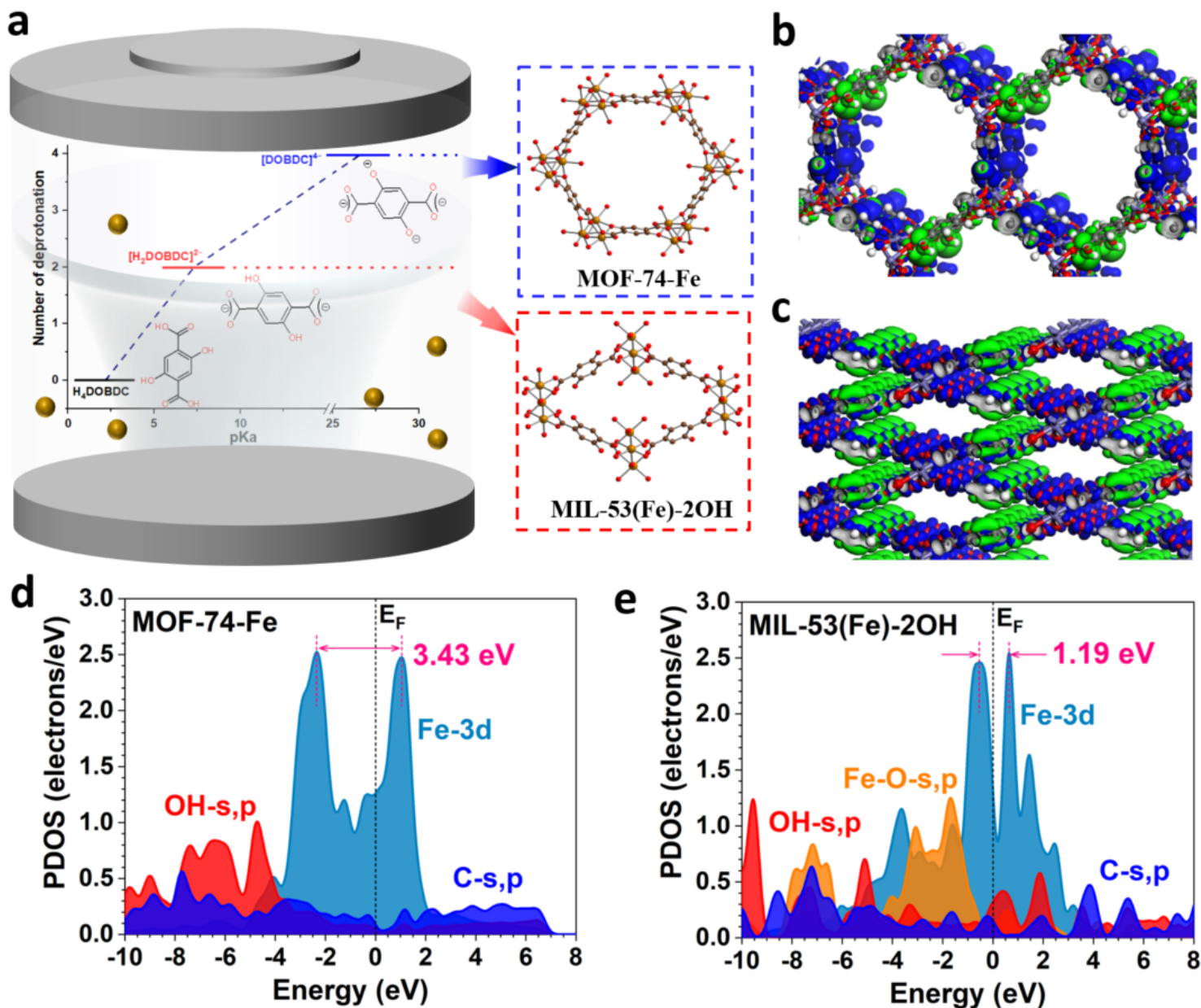


Figure 1

Synthetic strategy for modulating the reconstruction of the MIL-53(Fe)-2OH and MOF-74-Fe catalysts. (a) Schematic illustration of the fabricated MIL-53(Fe)-2OH and MOF-74-Fe catalysts by solvothermal reaction. Inset: Deprotonation of 2,5-dihydroxyterephthalic acid (H_4DOBDC) precursor to 2,5-dihydroxyterephthalato dianion ($[H_2DOBDC]^{2-}$) and 2,5-dioxidoterephthalato tetra-anion ($[DOBDC]^{4-}$). Golden, red, brown, and white balls represent Fe, O, C and H atoms, respectively. The 3D contour plot of electronic distribution near Fermi level of (b) MOF-74-Fe and (c) MIL-53(Fe)-2OH. Blue balls = Fe, Grey balls = C, Red balls = O, and White balls = H. Blue Isosurface = bonding orbitals and green isosurface = anti-bonding orbitals. The PDOS comparison of (d) MOF-74-Fe and (e) MIL-53(Fe)-2OH.

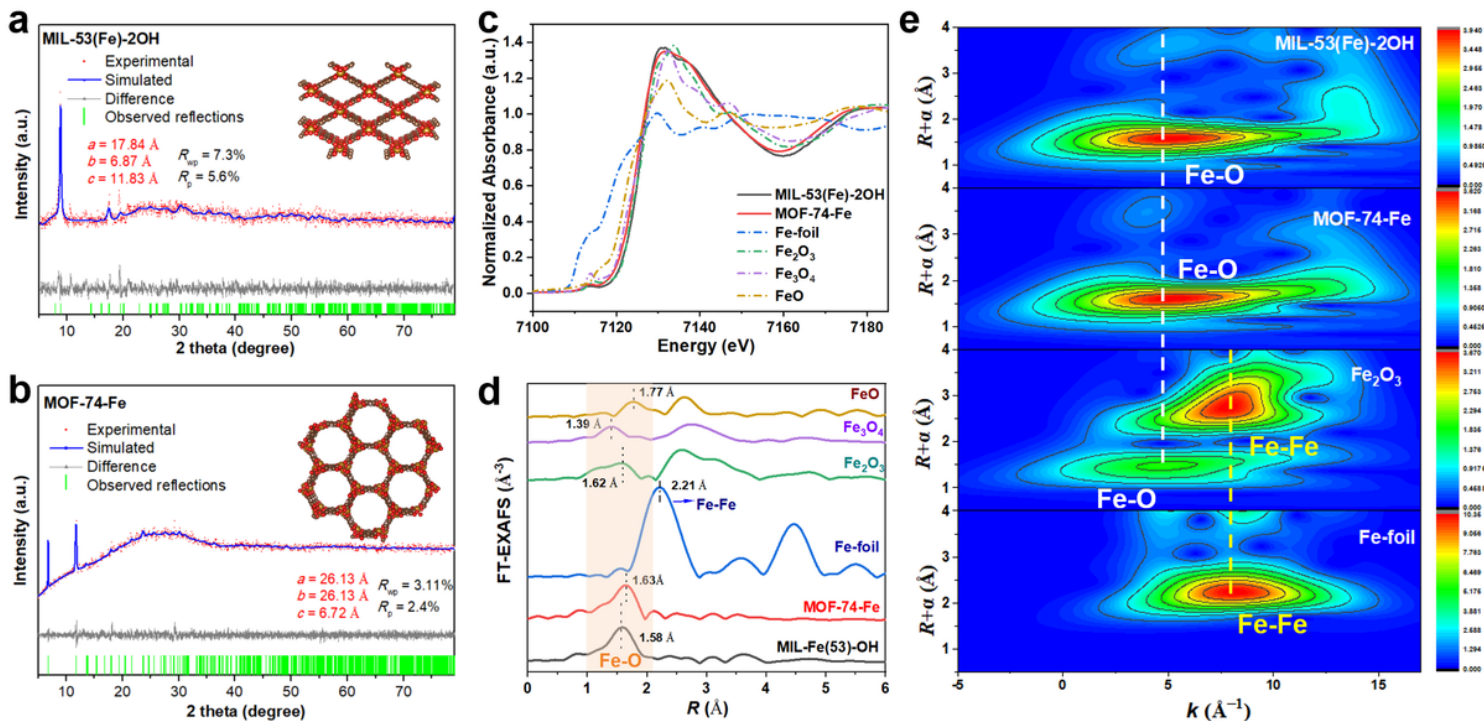


Figure 2

Structure characterization of the MIL-53(Fe)-2OH and MOF-74-Fe catalysts. Simulated and experimental XRD patterns of (a) MIL-53(Fe)-2OH and (b) MOF-74-Fe. Inset: corresponding schematic structure built using VESTA and refined using experimental XRD data. Golden, red, brown, and white balls represent Fe, O, C and H atoms, respectively. (c) Fe K-edge XANES spectra of MIL-53(Fe)-2OH, MOF-74-Fe, and its reference compounds. (d) FT-EXAFS spectra of the Fe K-for MIL-53(Fe)-2OH, MOF-74-Fe, and its reference compounds. (e) The wavelet transforms analysis of MIL-53(Fe)-2OH, MOF-74-Fe, Fe_2O_3 , and Fe-foil.

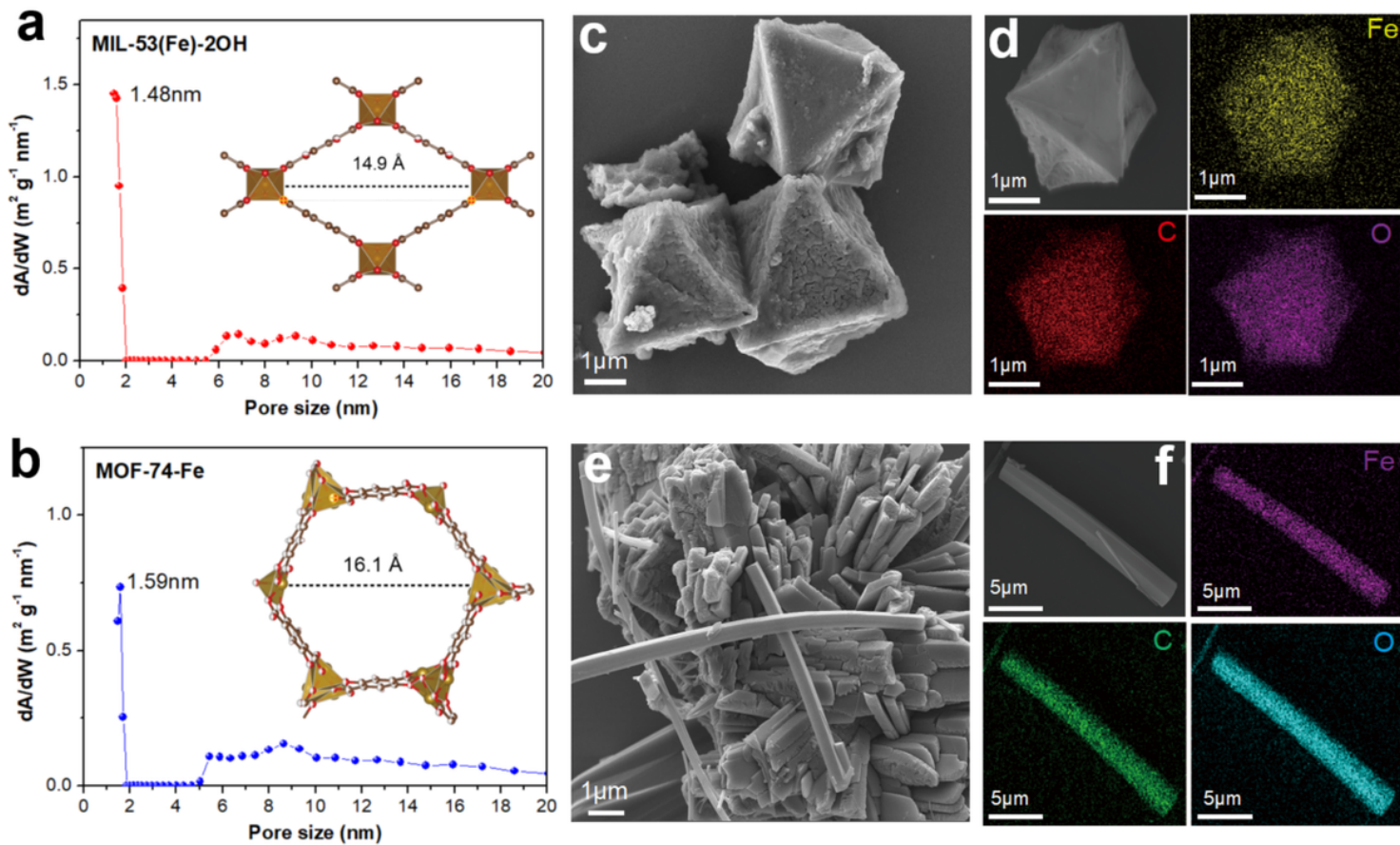


Figure 3

Morphology of the MIL-53(Fe)-2OH and MOF-74-Fe catalysts. Pore size distribution of (a) MIL-53(Fe)-2OH and (b) MOF-74-Fe. Inset: corresponding schematic structure of the catalysts based on the XRD analysis. (c) SEM image of MIL-53(Fe)-2OH and (d) the corresponding elements mapping for Fe, C, O. (e) SEM image of MOF-74-Fe and (f) the corresponding elements mapping for Fe, C, O.

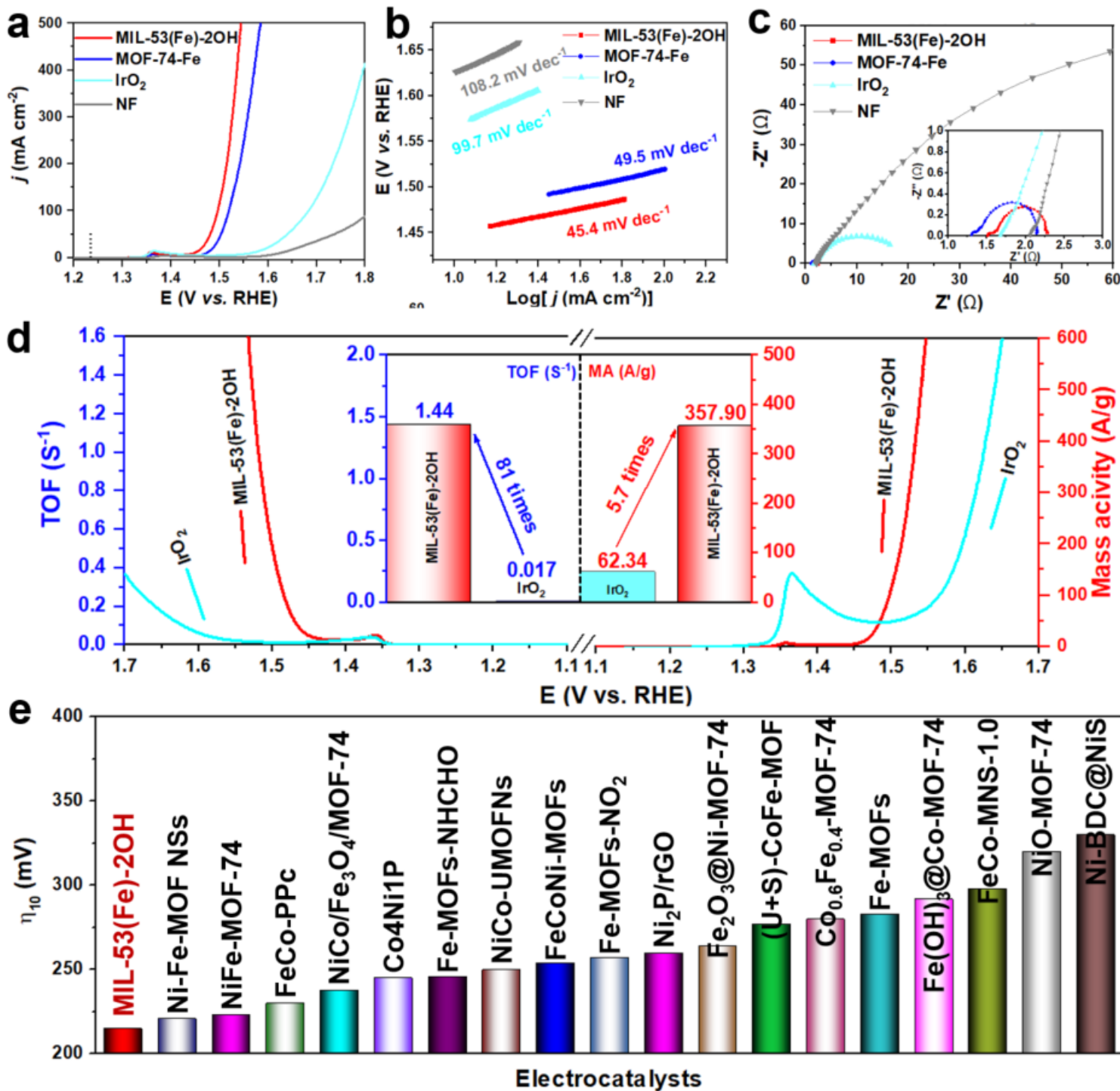


Figure 4

OER activity of the MIL-53(Fe)-2OH catalyst. (a) OER polarization curves of MIL-53(Fe)-2OH, MOF-74-Fe, IrO₂ and NF, and (b) the corresponding Tafel slopes. (c) Nyquist plots of MIL-53(Fe)-2OH, MOF-74-Fe, IrO₂ and NF measured at the overpotential of 300 mV. (d) Comparison of TOF and mass activity of the MIL-53(Fe)-2OH and IrO₂ catalysts at the overpotential of 300 mV. (e) Comparison of the oxygen evolution overpotential to drive a current density of 10 mA cm⁻² for the MIL-53(Fe)-2OH with other recently reported MOFs OER catalysts.

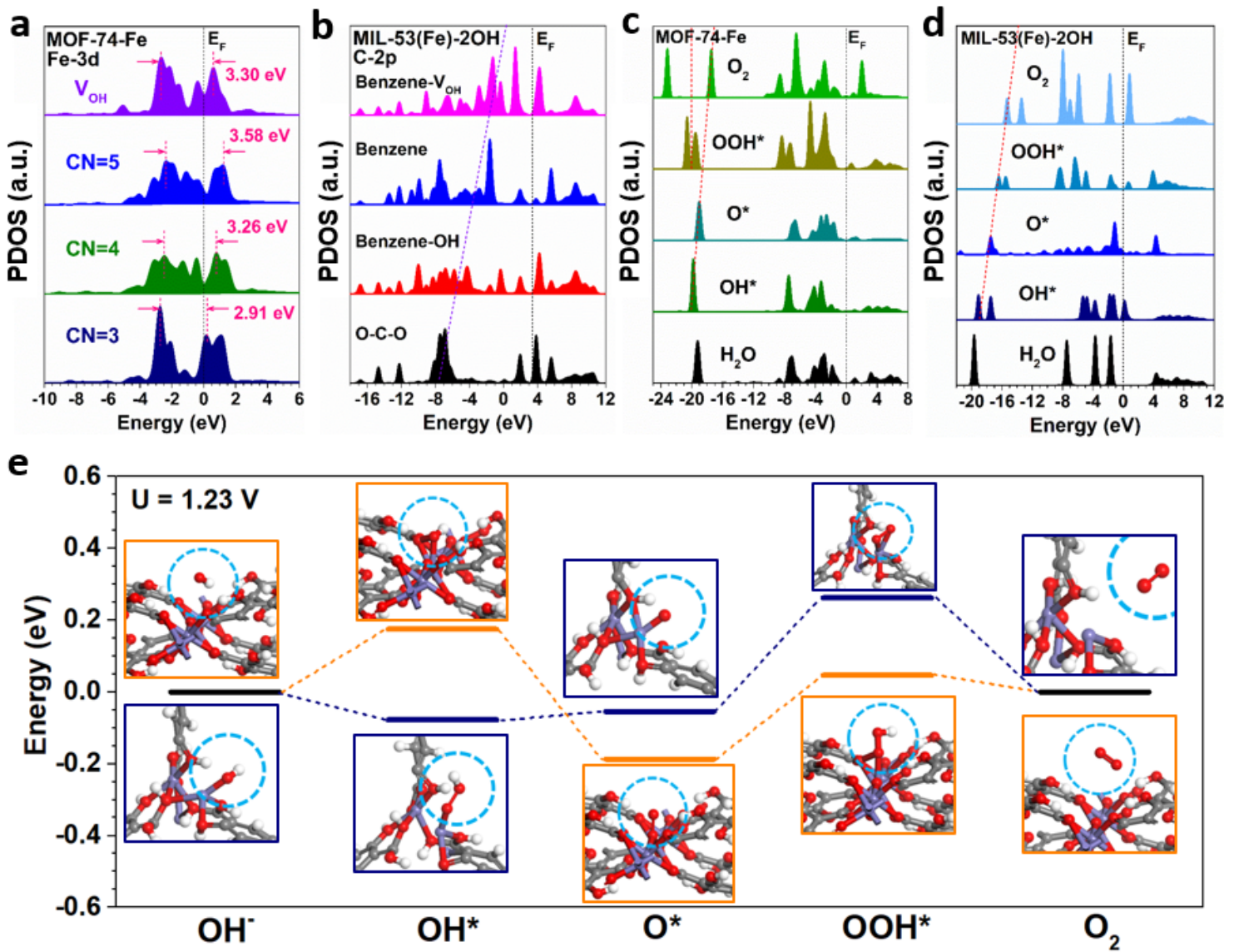


Figure 5

Theoretical calculations revealing mechanism for the high OER performance of MIL-53(Fe)-2OH. (a) The site-dependent PDOS of Fe-3d in MOF-74-Fe. (b) The site-dependent PDOS of C-2p in MIL-53(Fe)-2OH. The PDOS comparison of key adsorbates of OER in (c) MOF-74-Fe and (d) MIL-53(Fe)-2OH. (e) The reaction trend of ER under $U = 1.23$ V on MOF-74-Fe (blue line) and MIL-53(Fe)-2OH (orange line) with the corresponding structure changes of MOF-74-Fe (blue square) and MIL-53(Fe)-2OH (orange square).

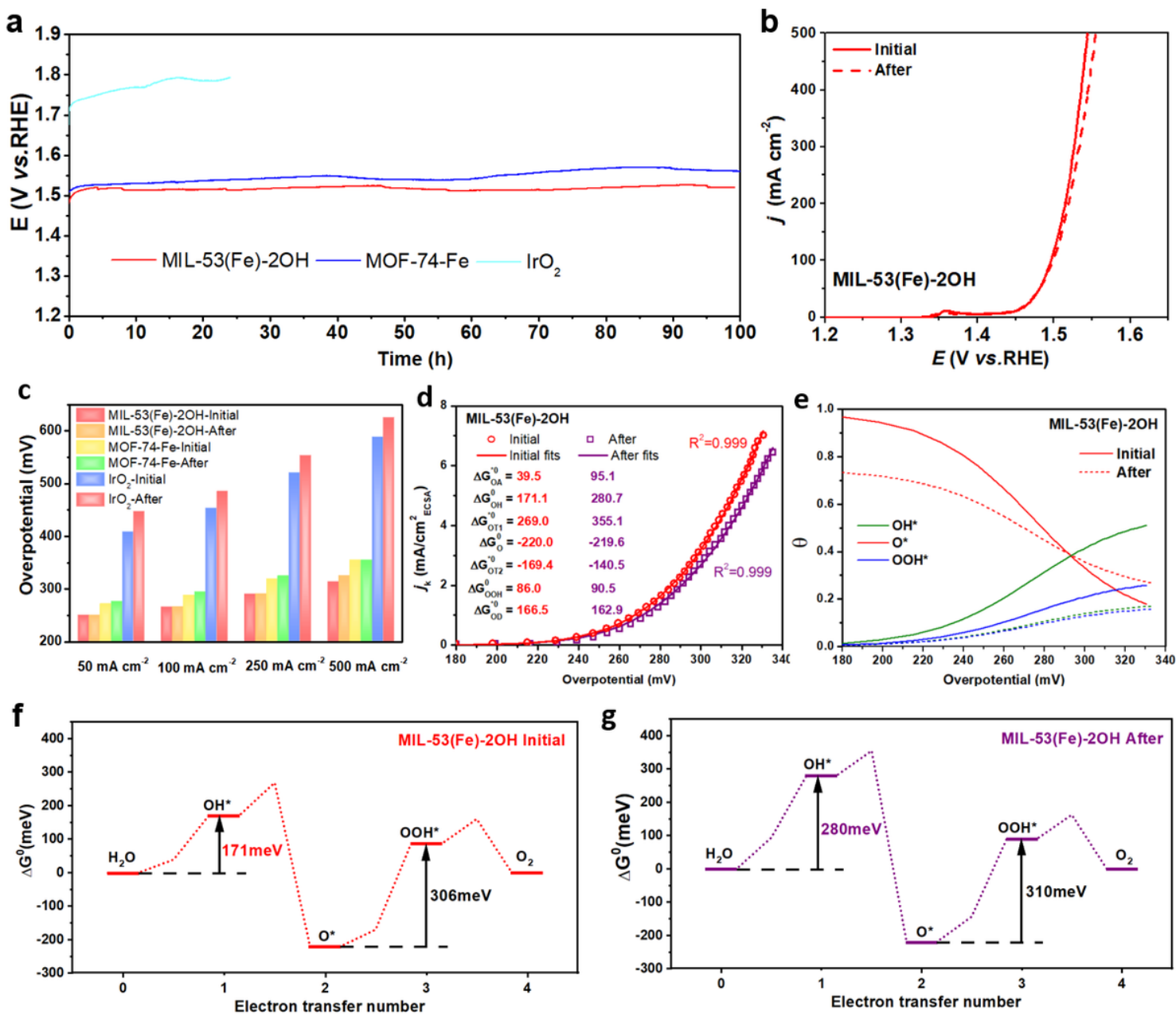


Figure 6

Stability Evaluation and the OER kinetics analysis of the MIL-53(Fe)-2OH catalyst. (a)

Chronopotentiometry responses ($E-t$) curves of the MIL-53(Fe)-2OH, MOF-74-Fe, and IrO_2 at the current density of 100 mA cm^{-2} for 100 hours. (b) Polarization curves of the MIL-53(Fe)-2OH before and after the stability tests at 100 mA cm^{-2} for 100 h. (c) Overpotential of FeCo-PPc, MOF-74-Fe and IrO_2 at different current densities before and after the stability tests. (d) Kinetic current density with the best OER kinetic fitting for the MIL-53(Fe)-2OH catalyst before and after the stability test. (e) Fractional coverage of the O^* , OH^* and OOH^* intermediates for MIL-53(Fe)-2OH catalyst before and after the stability test. Free energy diagram of the MIL-53(Fe)-2OH catalyst (f) before and (g) after the stability test with the dominant $4e^-$ pathway.

Supplementary Files

This is a list of supplementary files associated with this preprint. Click to download.

- [H4DOBDCMOFsOERSI20220730.docx](#)